ICRF Antenna Modeling and Coupling Analysis for CFEDR

Yuhao Jiang[1,2,*], *Chengming* Qin[1,**], *Wei* Zhang[1,***] *Lunan* Liu[1], *Zhengshuyan* Wang[1,2], *Yaoyao* Guo[1,2], *Xinjun* Zhang[1], *Lin* Ai[1,2], *Rui* Ding[1], *Vincent* Chan[1], *Jiale* Chen[1], *Xiaojie* Wang[1], *Guoliang* Xu[1], and *Jiangang* Li[1]

[1]Institute of Plasma Physics, Hefei Institutes of Physical Science, Chinese Academy of Sciences, Hefei 23001, China
[2]University of Science and Technology of China, Hefei 230026, China

Abstract. The Ion Cyclotron Range of Frequencies (ICRF) is an important auxiliary plasma heating method in the Chinese Fusion Engineering DEMO Reactor (CFEDR). A coupled ICRF power P_c of 10 MW during the ramp-up phase and 20 MW during the flat-top phase is required, launched from an ICRF antenna located at an equatorial port, to obtain or sustain conventional H-mode in CFEDR. Using the CFETR-ICRF antenna model by Zhang et al [10], we use RAPLICASOL code to evaluate ICRF wave coupling across various plasma conditions and toroidal phasings. The analysis of the antenna coupling resistance R_c, power spectrum, parallel wavenumber $k_\parallel$, surface current distribution on the straps J_s, and parallel electric field $E_\parallel$ under different edge electron density n_e profiles and toroidal phasings [$(0, \pi, 0, \pi, 0, \pi)$, $(0, \pi, \pi, 0, 0, \pi)$, and $(0, 0, \pi, \pi, 0, 0)$], for frequencies between 40 MHz and 90 MHz, are presented.

1 Introduction

Ion cyclotron resonance frequency (ICRF) heating is an effective auxiliary heating method in tokamak devices. It enables direct heating of target ions within tokamaks by adjusting relevant parameters. This positions ICRF heating as essential for future reactor ion heating, such as ITER [1–3], CFETR [4–6], and DEMO [7, 8].

The China Fusion Engineering DEMO Reactor (CFEDR) is the future magnetic confinement fusion DEMO reactor. The core objective of CFEDR is to validate the key technologies of DEMO-level fusion and develop Reliability, Availability, Maintainability, and Inspectability (RAMI) standards for critical systems. In the conventional H-mode phase in CFEDR, the main parameters are as follows: major radius R_0 = 7.8 m, minor radius a = 2.5 m, toroidal magnetic field B_t = 6.3 T, plasma current I_p = 15 MA, and safety factor q_{95} = 5.3, with a lower single null divertor configuration. Only one ICRF antenna will be installed at the equatorial port, which has an area of S_{port} = 6.864 m^2. Without limiters, the antenna is positioned flush with the first wall at R_{ant} = 10.5 m.

As previously noted, ICRF provides efficient direct ion heating without high density propagation limits. This characteristic ensures effective core power deposition via ICRF fast wave (FW) even in CFEDR's anticipated high-density operational regimes. Therefore, 10 MW of ICRF power is required to rapidly heat the plasma core during the ramp-up phase, in order to minimize the resistive losses and magnetic flux consumption. Meanwhile, in the flat-top phase, 20 MW of ICRF coupled power is needed for triggering and sustaining the conventional H-mode operation through low-to-high (LH) transition, as shown in figure 1.

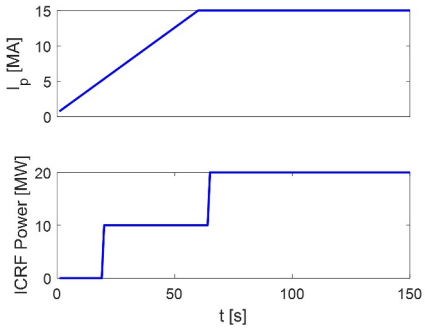

Figure 1. Plasma current and ICRF power against time during CFEDR operation. In ramp-up phase (20 < t < 60 s), ICRF is required to inject 10 MW; in flat-top phase (t > 60 s), ICRF is required to inject 20 MW.

There are three potential ICRF heating schemes during the conventional H-mode phase with deuterium-tritium (D-T) plasma: 1. lithium-7 (^{7}Li) minority heating with an ICRF frequency of 39 MHz; 2. helium-3 (^{3}He) minority heating around 60 MHz; and 3. hydrogen (H) minority heating around 90 MHz, which have been investigated for core power absorption [9], as shown in Figure 2. In addition, the geometry and structure of the ICRF antenna have been previously optimized by Zhang et al. using the RAPLICASOL antenna code [10]. The analysis indicates that an ITER-like antenna configuration with 4 poloidal sub-straps and 6 toroidal strap columns (per half antenna) can offer the most effective strategy for coupling power to

*Corresponding author: yuhao.jiang@ipp.ac.cn
**Corresponding author: chmq@ipp.ac.cn
***Corresponding author: wei.zhang@ipp.ac.cn

the plasma. This arrangement results in the highest coupling resistance and the lowest transmission line voltage, while also minimizing the electric field intensity on the strap surfaces. Subsequent parametric scans identified the optimal geometric dimensions of the antenna as follows: strap height $H_{\text{strap}} = 0.29, \text{m}$, strap width $W_{\text{strap}} = 0.21, \text{m}$, strap depth $d_{\text{strap}} = 0.29, \text{m}$, and connection bridge depth $d_{\text{con}} = 0.18, \text{m}$. The overview of the antenna and the strap is shown in figure 3. Since CFEDR and CFETR share the same equatorial port dimensions, the same ICRF antenna geometry as that of CFETR is adopted in the simulations. The antenna has 2.250 m width and 2.700 m height, corresponding to an area of approximately $S = 6.075\,\text{m}^2$.

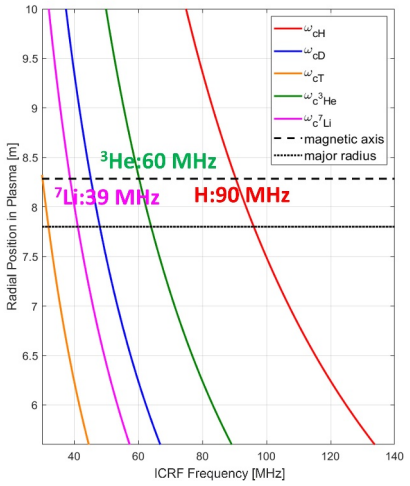

Figure 2. Fundamental resonance positions versus ICRF frequency. At the magnetic axis (the long dashed line), the resonance frequencies are 39 MHz (^{7}Li), 60 MHz (^{3}He), and 90 MHz (H).

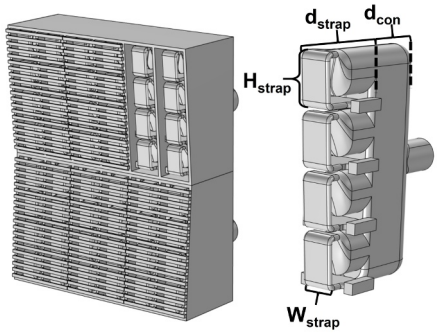

Figure 3. Overview of the antenna and the strap.

We evaluate the performance of an optimized ICRF antenna using a realistic full antenna model for the three potential heating schemes. Leveraging the RAPLICASOL code and simulated edge density profiles, the research focuses on assessing antenna behavior during the conventional H-mode phase across various edge plasma conditions to optimize the toroidal phasing configurations. The evaluation quantifies antenna coupling capability through calculations of coupling resistance (R_c) and examines surface current distributions (J_{sy}) on straps. Analysis of the ICRF wave power spectrum ($k_{\|}$) enables cross-verification with core absorption mechanisms, while computation of the parallel electric field ($E_{\|}$) near the antenna face provides preliminary assessment of sheath-induced effects relevant to impurity production. The paper is structured as follows: Section 2 introduces the fundamental simulation setups and governing equations. Section 3 presents antenna simulation results and analysis. Section 4 summarizes conclusions.

2 Simulation setups

2.1 Physical parameters

The density and temperature profiles of ions and electrons are presented in figure 4. These correspond to a baseline scenario prior to the application of any specific ICRF heating scheme. These profiles are derived from integrated modeling of CFEDR conventional H-mode operation [11], with core electron temperature $T_{e0} = 30\,\text{keV}$, ion temperature $T_{i0} = 24\,\text{keV}$, and density $n_{e0} = 1.5 \times 10^{20}\,\text{m}^{-3}$. Furthermore, the electron density at the last closed flux surface (LCFS) is $n_{e1} = 0.39 \times 10^{20}\,\text{m}^{-3}$.

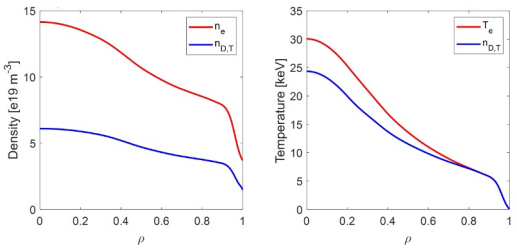

Figure 4. Electron (red) and ion (black) density and temperature profiles in conventional H-mode phase.

Figure 5 shows the density profile in the scrape-off layer (SOL). In our simulations, we utilize three density profiles that share the same electron density at LCFS ($n_{e1} = 0.39 \times 10^{20}\,\text{m}^{-3}$), but exhibit different densities at the antenna location: high-density case (blue) $n_{e,\text{ant,h}} = 1.15 \times 10^{18}\,\text{m}^{-3}$; medium-density case (red) $n_{e,\text{ant,m}} = 6.03 \times 10^{17}\,\text{m}^{-3}$; low-density case (yellow) $n_{e,\text{ant,l}} = 5.57 \times 10^{16}\,\text{m}^{-3}$. The radial dependence of the toroidal magnetic field follows $B(r) = B_t \cdot R_0/r$, where $B_t = 6.3\,\text{T}$ and $R_0 = 7.8\,\text{m}$.

2.2 Antenna model

RAPLICASOL is an antenna coupling code based on COMSOL software and the Finite Element Method [12]. It is used to calculate the scattering matrix, surface currents on the straps, radio frequency (RF) wave fields and other quantities, which are in good agreement with other codes [13]. All simulations in this article use the cold plasma approximation. In other words, the dispersion relations of plasma are expressed by the Stix dielectric tensor [14].

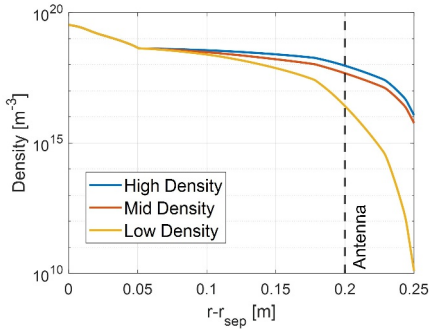

Figure 5. Electron density profiles in SOL sharing identical density at LCFS ($n_{e1} = 0.39 \times 10^{20}\,\mathrm{m}^{-3}$). At the antenna, in high-density case, $n_{e,\mathrm{ant,h}} = 1.15 \times 10^{18}\,\mathrm{m}^{-3}$; in medium-density case: $n_{e,\mathrm{ant,m}} = 6.03 \times 10^{17}\,\mathrm{m}^{-3}$; in low-density case: $n_{e,\mathrm{ant,l}} = 5.57 \times 10^{16}\,\mathrm{m}^{-3}$.

Figure 4, 6 shows the full geometry of the realistic antenna model. The antenna consists of upper and lower halves. Each half is composed of a 4×6 (poloidal $\times$ toroidal) array. Each strap column integrates a water tank for cooling and neutron shielding, and connects to a transmission line with characteristic impedance of 25 Ω. Faraday screen is located on the antenna strap front of 1cm for mitigating the RF sheath potential induced by slow wave (SW). To better fit both the plasma boundary and first wall, the upper and lower antenna sections are angled at 7.96° relative to each other. Figure 6 also displays top and side views of the full simulation model. The antenna is fully encapsulated in vacuum, separated from a cold plasma layer by a 2 cm gap. The entire model is bounded by a 5 cm thick perfect matching layer (PML).

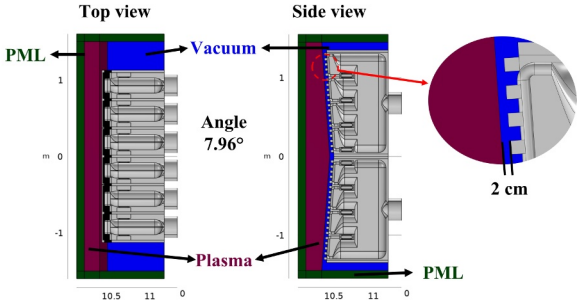

Figure 6. Top and side views of the antenna model in the simulation.

3 Simulation results

In this section, simulations have been conducted using three different toroidal phasing configurations under varying electron density profiles: $(0, \pi, 0, \pi, 0, \pi)$, $(0, \pi, \pi, 0, 0, \pi)$, and $(0, 0, \pi, \pi, 0, 0)$. The phasing between the upper and lower straps is set to $(0, \pi)$ by default. For all the heating schemes discussed above, the operating frequency was also scanned from 30 MHz to 90 MHz.

3.1 Power spectrum and cut-off density

Through analysis of the FW field distribution at the antenna aperture and subsequent Fourier transform, the power spectrum of the ICRF wave for each toroidal phasing is obtained, as shown in figure 7. The dominant parallel wavenumber $k_\parallel$ depends on the toroidal spacing between straps S_z and the phase difference $\Delta\phi$ between adjacent straps via $k_\parallel = \frac{\Delta\phi}{S_z}$. Therefore, different toroidal phasings result in distinct $k_\parallel$ values. The maximum $k_\parallel = 8.1\ \mathrm{m}^{-1}$ occurs for $(0, \pi, 0, \pi, 0, \pi)$, followed by $4.5\ \mathrm{m}^{-1}$ for $(0, \pi, \pi, 0, 0, \pi)$, and the minimum of $3.3\ \mathrm{m}^{-1}$ for $(0, 0, \pi, \pi, 0, 0)$.

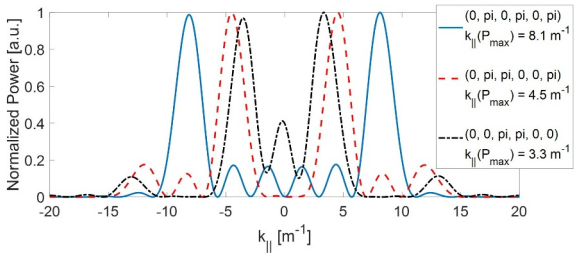

Figure 7. Power spectrum for three toroidal phasing configurations. The dominant $k_\parallel$ values are $8.1\ \mathrm{m}^{-1}$ for $(0, \pi, 0, \pi, 0, \pi)$, $4.5\ \mathrm{m}^{-1}$ for $(0, \pi, \pi, 0, 0, \pi)$, and $3.3\ \mathrm{m}^{-1}$ for $(0, 0, \pi, \pi, 0, 0)$.

In the $(0, 0, \pi, \pi, 0, 0)$ case, the two central-straps share the same phase, resulting not only in a lower $k_\parallel$ but also non-zero power at $k_\parallel = 0$. These low $k_\parallel$ modes, associated with coaxial modes, should be avoided due to their poor power absorption. Indeed, for efficient core heating in conventional H-mode operation, $k_\parallel$ should exceed $4\ \mathrm{m}^{-1}$ [9]. Moreover, the coupling resistance scales as $R_c \propto \exp(-\alpha\, k_\parallel\, d_{evan})$, where α is the tunneling factor and d_{evan} is the evanescent distance from the antenna to the cut-off layer. Thus, higher $k_\parallel$ directly reduces coupling and increases the FW cut-off density ($n_{e,co}$), thereby extending the evanescent distance (d_{evan}), degrading coupling efficiency, and raising sheath potentials at the antenna aperture.

Figure 8 shows that $n_{e,co}$ decreases with increasing ICRF frequency, and for a given frequency, higher $k_\parallel$ corresponds to a higher $n_{e,co}$. These results, as well as those in table 1, are obtained using the same electron and ion density/temperature profiles for all cases, while varying only the plasma composition to represent different heating schemes. Table 1 summarizes, at $f_{\mathrm{ICRF}} = 60$ MHz (^{3}He minority heating) and $f_{\mathrm{ICRF}} = 90$ MHz (H minority heating), the furthest (with $(0, \pi, 0, \pi, 0, \pi)$ phasing in low density) and nearest (with $(0, 0, \pi, \pi, 0, 0)$ phasing in high density) distances from the cut-off layer to the antenna front face for the extreme density profiles.

3.2 Maximum voltage and coupling resistance

In each half of the antenna, there are six toroidal strap columns corresponding to six transmission-line feeds, as shown in figure 9. The color assigned to each port will be

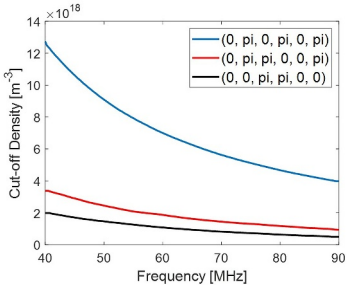

Figure 8. $n_{e,co}$ versus ICRF frequency. For a given frequency, configurations with smaller $k_\parallel$ yield lower $n_{e,co}$.

Table 1. Distances from the cut-off layer to the antenna front face for the furthest (with $(0,\pi,0,\pi,0,\pi)$ phasing in low density) and nearest (with $(0,0,\pi,\pi,0,0)$ phasing in high density) at $f_{\mathrm{ICRF}} = 60$ MHz and $f_{\mathrm{ICRF}} = 90$ MHz.

State	Heating scheme	Distance [cm]
Furthest	D–T(^{3}He) ~ 60 MHz	15.7
	D–T(H) ~ 90 MHz	12.5
Nearest	D–T(^{3}He) ~ 60 MHz	7.3
	D–T(H) ~ 90 MHz	4.5

used consistently in the figures below. The coupled power on each strap column is assumed equal, i.e., $P_i - P_j = 0$ $(i \neq j)$, where the subscript denotes the i-th (or j-th) feed line. From the simulated S-matrix and by imposing a maximum voltage of all RF feeding lines of $V_{\text{stand-off}} = 35$ kV, one can compute the antenna's equivalent coupling resistance and the maximum voltage at each port.

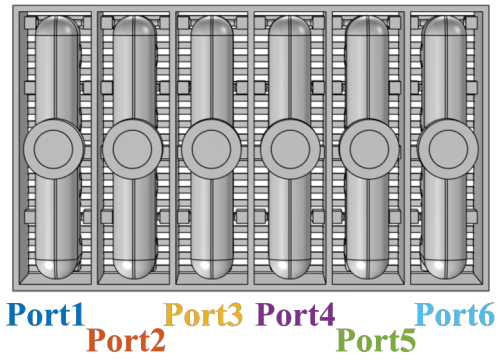

Figure 9. Half-antenna model showing six toroidal strap columns connected to transmission-line ports, each feeding a 25 Ω line.

Figure 10 shows the maximum voltage $V_{\max}$ at each port for the mid-density profile under various toroidal phasings and frequencies. The port colors and positions correspond to those in figure 9. Dashed lines represent the central-straps, solid lines the side-straps, and dotted lines the intermediate straps.

It is evident that for the $(0,\pi,0,\pi,0,\pi)$ and $(0,\pi,\pi,0,0,\pi)$ phasings, the central-straps consistently require higher voltage (input power) to couple the same power to the plasma, whereas the side-straps require significantly less. This indicates that the coupling capability of the central-straps is lower than that of the side-straps in these configurations. Conversely, for the $(0,0,\pi,\pi,0,0)$ phasing, the side-straps exhibit poorer coupling and thus demand higher voltage to deliver the same power. Such a feeding pattern enhances the parallel electric field $(E_\parallel)$ at the antenna sides, increasing the sheath potential — an effect that will be discussed in the next section.

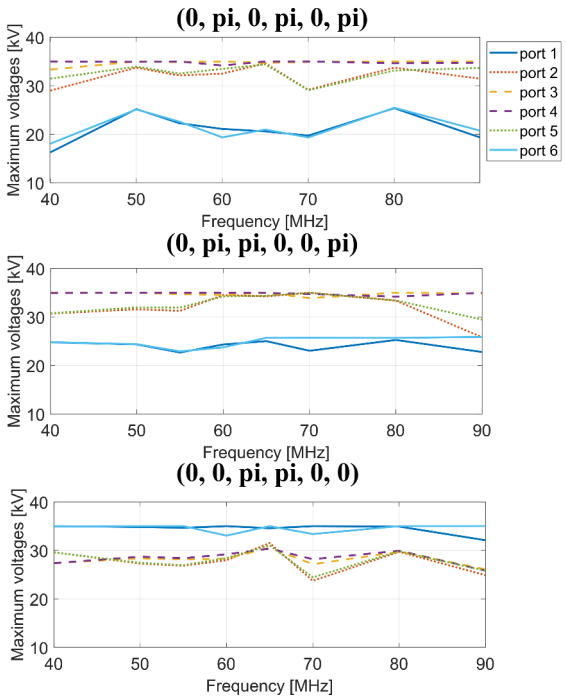

Figure 10. Maximum voltage $V_{\max}$ per port under different toroidal phasings and frequencies for the mid-density profile. Solid: side-straps; dashed: central-straps; dotted: intermediate straps.

Figure 11 illustrates the antenna coupling resistance R_c as a function of ICRF frequency for three toroidal phasings: solid line for $(0,\pi,0,\pi,0,\pi)$, dotted line for $(0,\pi,\pi,0,0,\pi)$, and dashed line for $(0,0,\pi,\pi,0,0)$. The blue, red, and orange traces correspond to the high, mid, and low density profiles, respectively.

The $(0,0,\pi,\pi,0,0)$ phasing exhibits the highest R_c, due to its lowest parallel wavenumber $k_\parallel$, while the $(0,\pi,0,\pi,0,\pi)$ phasing, with the highest $k_\parallel$, yields the lowest R_c. Across density cases, the high-density profile achieves the largest R_c, as the antenna is closest to the FS cut-off layer. Notably, two pronounced peaks in R_c occur near 60 MHz and 90 MHz, corresponding to the ^{3}He and H minority resonance frequencies. These results not only confirm the antenna optimization reported by Zhang et al [10], but also suggest that the water tank section of the transmission line acts as an impedance transformer, establishing effective operating bands around 60 and 90 ±10 MHz.

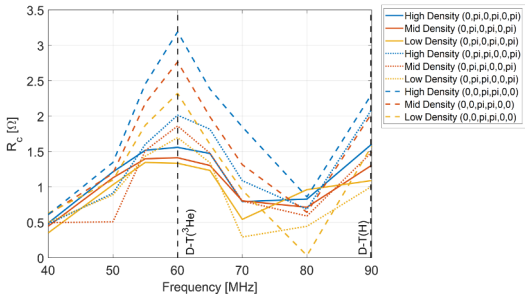

Figure 11. Coupling resistance R_c versus ICRF frequency for three toroidal phasings: solid $(0,\pi,0,\pi,0,\pi)$, dotted $(0,\pi,\pi,0,0,\pi)$, dashed $(0,0,\pi,\pi,0,0)$. Colors denote high (blue), mid (red), and low (orange) density profiles.

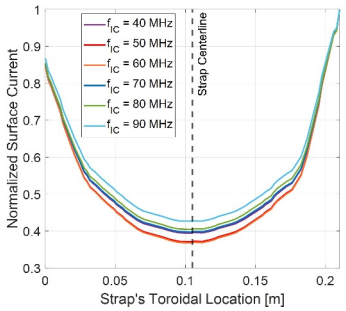

Figure 13. Normalized poloidal integration of J_{sy} for all straps in each toroidal column at various frequencies. The horizontal axis represents the strap's toroidal location.

3.3 Surface current and parallel electric field

Figure 12 presents the full-antenna surface current distribution J_{sy} under the $(0,\pi,0,\pi,0,\pi)$ phasing, alongside a zoomed-in view of a single strap. Figure 13 shows the normalized poloidal integration of J_{sy} over all straps in each toroidal column, plotted against the strap's toroidal location. The strap geometry remains fixed, and the curves illustrate how the surface current distribution varies with frequency.

The normalized surface current distribution (see Figure 13) appears relatively uniform across the straps in our segmented-strap (short sub-strap) antenna configuration. This phenomenon may be associated with the segmentation of the antenna into multiple short sub-straps—a design strategy adopted in ITER-like antennas, which has been suggested in previous studies to improve current distribution and radiation performance [16, 17]. However, since no direct comparison with longer strap configurations is presented here, the influence of strap segmentation on current uniformity and overall antenna performance cannot be conclusively demonstrated in this work.

Localized peaks in Figure 12 are mesh refinement artifacts caused by cooling channels and structural thickness; these do not reflect physical nonuniformities, as indicated by the integrated profiles in Figure 13.

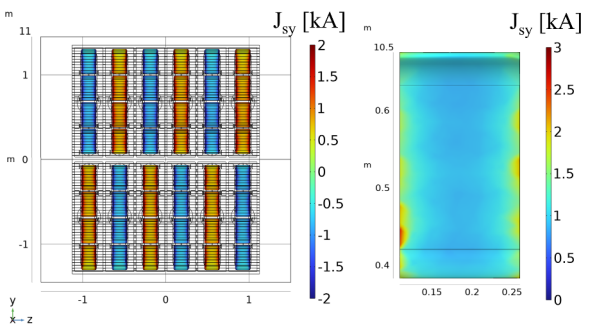

Figure 12. Surface current distribution J_{sy} on all straps of the full antenna with $(0,\pi,0,\pi,0,\pi)$ phasing, and a zoomed detail on a single strap.

The minimization of the parallel RF electric field $E_\parallel$ on the antenna's lateral sides is critical, as it serves as an indicator of RF sheath rectification, which enhances ion sputtering and increases heat loads. This is especially important for all-tungsten tokamak devices, where large RF sheaths can scatter tungsten impurities into the core plasma, degrading performance. In this study, the feeding voltages are taken from the results of figure 10 by enforcing equal coupled power on each strap column.

Figure 14 then shows the spatial distribution of $E_\parallel$ at 1 cm in front of the antenna for the mid-density profile at an ICRF frequency of 60 MHz under the three phasings $(0,\pi,0,\pi,0,\pi)$, $(0,\pi,\pi,0,0,\pi)$, and $(0,0,\pi,\pi,0,0)$. The field concentrates and intensifies at the antenna edges, whereas in the central region $E_\parallel$ is more uniform, indicating the action of the Faraday bars in reducing sheath potentials. Overall, the $(0,\pi,\pi,0,0,\pi)$ phasing yields the lowest $\langle E_\parallel \rangle$.

To quantify the comparison, we compute the mean absolute parallel electric field $\langle |E_\parallel| \rangle$ on both lateral sides of the antenna, with the selected region shown in figure 15(a). The results are presented in figure 15(b), where the left panel summarizes $\langle |E_\parallel| \rangle$ for ^{3}He minority heating (60 MHz) across different toroidal phasings and density profiles, and the right panel shows the H minority case (90 MHz). The results reveal three main trends:

- **Frequency and density profile:** The ICRF frequency and edge density directly affect coupling, and thus the slow-wave–dominated $\langle |E_\parallel| \rangle$. For example, at 60 MHz with high density, the $(0,\pi,0,\pi,0,\pi)$ phasing yields $\langle |E_\parallel| \rangle = 8.764$ kV/m, substantially lower than the 25.164 kV/m obtained at low density, and also lower than the 9.807 kV/m at 90 MHz high density.
- **Toroidal phasing:**
  - Comparing $(0,\pi,0,\pi,0,\pi)$ and $(0,\pi,\pi,0,0,\pi)$: the latter has higher coupling efficiency, so its $\langle |E_\parallel| \rangle$ is lower. At 60 MHz high density, $(0,\pi,\pi,0,0,\pi)$ gives 3.359 kV/m versus 8.764 kV/m for $(0,\pi,0,\pi,0,\pi)$.
  - Comparing either of the above with $(0,0,\pi,\pi,0,0)$: although this phasing has a larger coupling resistance, the side-straps require more input voltage (and thus higher local $E_\parallel$) to equalize coupled power.

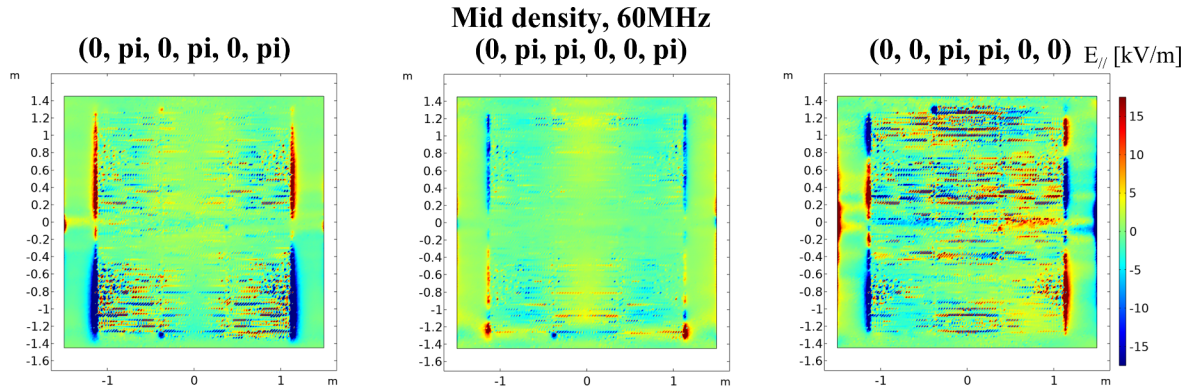

Figure 14. $E_{\|}$ distribution at 1 cm in front of the antenna for the mid-density profile and 60 MHz ICRF under phasings $(0,\pi,0,\pi,0,\pi)$, $(0,\pi,\pi,0,0,\pi)$, and $(0,0,\pi,\pi,0,0)$. The apparent irregularities in front of the FS are due to numerical resolution limits (mesh size) rather than physical effects.

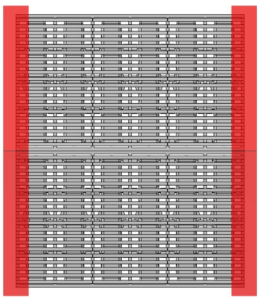

(a)

^{3}He minority (60MHz)

Toroidal phasing	Poloidal phasing	Density	<|E//,lim|> [kV/m]
(0, pi, 0, pi, 0, pi)	(0, pi)	High density	8.7640
		Mid density	9.2508
		Low density	25.1643
(0, pi, pi, 0, 0, pi)		High density	3.3586
		Mid density	3.7601
		Low density	11.2980
(0, 0, pi, pi, 0, 0)		High density	15.6891
		Mid density	18.1415
		Low density	35.8645

H minority (90MHz)

Toroidal phasing	Poloidal phasing	Density	<|E//,lim|> [kV/m]
(0, pi, 0, pi, 0, pi)	(0, pi)	High density	9.8070
		Mid density	10.3974
		Low density	17.4300
(0, pi, pi, 0, 0, pi)		High density	5.4096
		Mid density	5.6787
		Low density	20.5800
(0, 0, pi, pi, 0, 0)		High density	22.0234
		Mid density	26.9283
		Low density	47.9535

(b)

Figure 15. (a). Definition of the lateral side area used for $\langle|E_{\|}|\rangle$ calculation. (b). Mean absolute parallel RF electric field $\langle|E_{\|}|\rangle$ on the antenna sides. Left: ^{3}He minority heating (60 MHz) for various toroidal phasings and density profiles. Right: H minority heating (90 MHz) results.

Hence $\langle|E_{\|}|\rangle$ increases. At 60 MHz high density, $(0,0,\pi,\pi,0,0)$ produces 15.689 kV/m, exceeding the values for the other two phasings.

4 Conclusion

Coupling modeling and analysis for an optimized ITER-type ICRF antenna for CFEDR were conducted using the RAPLICASOL code and realistic edge plasma profiles. Antenna coupling behavior was evaluated for various heating schemes and toroidal phasings.

The results demonstrated that toroidal phasing significantly affects both the coupling resistance (R_c) and the power spectrum. The $(0,0,\pi,\pi,0,0)$ phasing exhibited the highest R_c due to its lowest parallel wavenumber ($k_{\|}$), whereas $(0,\pi,0,\pi,0,\pi)$ presented the lowest R_c and the highest $k_{\|}$. Generally, lower $k_{\|}$ values correspond to lower cut-off densities ($n_{e,\mathrm{co}}$), improving coupling efficiency and decreasing $\langle|E_{\|}|\rangle$ near the antenna. However, this was not the case for the $(0,0,\pi,\pi,0,0)$ phasing, as higher voltages on the side straps were required to achieve equal coupled power among all strap columns. Analysis of the parallel electric field ($E_{\|}$) indicated minimal sheath potentials, particularly for the $(0,\pi,\pi,0,0,\pi)$ phasing at high densities. The ITER-type antenna shows relatively uniform surface current distribution across the straps, suggesting good current sharing and power-handling potential. However, further work is needed to quantitatively assess the impact of sub-strap segmentation.

Based on a comprehensive analysis of these factors, the $(0,0,\pi,\pi,0,0)$ phasing emerges as the most promising option for future ICRF heating in CFEDR. These findings validate the ITER-like antenna design for CFEDR and emphasize the importance of careful phasing and density profile management to optimize performance. They provide key guidance for future ICRF antenna designs.

References

[1] P. Dumortier et al., RF optimization of the ITER ICRF antenna plug including its broad banding by a service stub, Fusion Eng. Des. **84**, 707 (2009). https://doi.org/10.1016/j.fusengdes.2008.11.101

[2] A. Messiaen et al., Performance of the ITER ICRH system as expected from TOPICA and ANTITER II modelling, Nucl. Fusion **50**, 025026 (2010). https://doi.org/10.1088/0029-5515/50/2/025026

[3] D. Milanesio et al., ITER ICRF antenna analysis and optimization using the TOPICA code, Nucl. Fusion **50**, 025007 (2010). https://doi.org/10.1088/0029-5515/50/2/025007

[4] Y. Song et al., Concept design on RH maintenance of CFETR Tokamak reactor, Fusion Eng. Des. **89**, 2331 (2014). https://doi.org/10.1016/j.fusengdes.2014.03.045

[5] B. N. Wan et al., Physics Design of CFETR: Determination of the Device Engineering Parameters, IEEE Trans. Plasma Sci. **42**, 495-(2014). https://doi.org/10.1109/TPS.2013.2296939

[6] J. Li et al., Present State of Chinese Magnetic Fusion Development and Future Plans, J. Fusion Energ. **38**, 113 (2019). https://doi.org/10.1007/s10894-018-0165-2

[7] V. Bobkov et al., Development of pre-conceptual ITER-type ICRF antenna design for DEMO, Nucl. Fusion **61**, 046039 (2021). https://doi.org/10.1088/1741-4326/abe7d0

[8] M. Q. Tran et al., Status and future development of Heating and Current Drive for the EU DEMO, Fusion Eng. Des. **180**, 113159 (2022). https://doi.org/10.1016/j.fusengdes.2022.113159

[9] Y. Jiang et al., Simulation analysis of ICRF heating scenarios for CFEDR, Plasma Sci. Technol. **27**, 104012 (2025). https://doi.org/10.1088/2058-6272/adfef5

[10] W. Zhang et al., Conceptual design and optimization of an ITER-type ICRF antenna on CFETR, Nucl. Fusion **62**, 076045 (2022). https://doi.org/10.1088/1741-4326/ac6681

[11] R. Ding et al., 1st CFEDR Physical Design IAC Meeting, Hefei, China, 29–30 October 2024.

[12] J. Jacquot et al., Full wave propagation modelling in view to integrated ICRH wave coupling/RF sheaths modelling, AIP Conf. Proc. **1689**, 050008 (2015). https://doi.org/10.1063/1.4936496

[13] W. Tierens et al., Validation of the ICRF antenna coupling code RAPLICASOL against TOPICA and experiments, Nucl. Fusion **59**, 046001 (2019). https://doi.org/10.1088/1741-4326/aaf455

[14] T. H. Stix, Waves in Plasmas, (American Institute of Physics, Melville, NY, 1992).

[15] S. Ceccuzzi et al., The ICRF antenna of DTT: Design status and perspectives Available, AIP Conf. Proc. **2984**, 030015 (2023). https://doi.org/10.1063/5.0162417

[16] V. Maquet et al., Preliminary RF characterization of DEMO in-port ion cyclotron heating system for toroidal and poloidal geometry variations, Fusion Eng. Des. **169**, 112508 (2021). https://doi.org/10.1016/j.fusengdes.2021.112508

[17] A. Messiaen et al., Modeling of the Traveling Wave Antenna in view of the ICRF heating of DEMO, EPJ Web Conf. **157**, 03033 (2017). https://doi.org/10.1051/epjconf/201715703033